AGU100 ADVANCING EARTH AND SPACE SCIENCE

Geophysical Research Letters

RESEARCH LETTER
10.1029/2018GL080399

Key Points:
- Submesoscale ageostrophic energy level experiences substantial variation through life cycle of mesoscale eddies
- Submesoscale ageostrophic energy level is relatively low in eddy's mature phase and high in both the formation and decaying phases
- Energy level of submesoscale ageostrophic motions depends positively on the local mesoscale deformation strain rate

Supporting Information:
- Supporting Information S1

Correspondence to:
B. Qiu,
bo@soest.hawaii.edu

Citation:
Zhang, Z., & Qiu, B. (2018). Evolution of submesoscale ageostrophic motions through the life cycle of oceanic mesoscale eddies. *Geophysical Research Letters*, *45*. https://doi.org/10.1029/2018GL080399

Received 7 SEP 2018
Accepted 14 OCT 2018
Accepted article online 19 OCT 2018

Evolution of Submesoscale Ageostrophic Motions Through the Life Cycle of Oceanic Mesoscale Eddies

Zhengguang Zhang[1,2] **and Bo Qiu**[3]

[1]Physical Oceanography Lab, Qingdao Collaborative Innovation Center of Marine Science and Technology, Ocean University of China, Qingdao, China, [2]Laboratory for Ocean and Climate Dynamics, Qingdao National Laboratory for Marine Science and Technology, Qingdao, China, [3]Department of Oceanography, University of Hawai'i at Mānoa, Honolulu, HI, USA

Abstract The global ocean circulation is forced by large-scale fluxes at the surface and dissipated at small scales by diffusion. To achieve a long-term equilibrium requires a dynamical route that transfers energy from large to dissipative scales. The submesoscale ageostrophic motions (1–50 km) have been hypothesized recently to play a critical role in this route by extracting energy from mesoscale eddies (50–500 km) that contain the majority of oceanic kinetic energy. By combining global surface velocity measurements by drifters and satellite altimeter-tracked eddy data set, we show that the submesoscale ageostrophic kinetic energy exhibits unexpected global mean features through the life cycle of mesoscale eddies. The ageostrophic energy is relatively small in eddy's mature phase but is large both in formation/decaying phases. Furthermore, the energy level of ageostrophic motions depends positively on the local geostrophic strain rate, suggesting that the geostrophic deformation field may dictate the energy transfer from mesoscale eddies to submesoscale motions.

Plain Language Summary Oceanic mesoscale eddies are energetic vortices with radius ranging from tens to hundreds of kilometers. These eddies contain the majority of the oceanic kinetic energy and play an important role in regulating oceanic transport of heat, salt, and other climatically important tracers. In order to understand the evolution of eddies through their life cycle, one key question that is yet to be fully answered is how the energy contained in the geostrophically balanced mesoscale eddies transfers to smaller scales where it can be dissipated irreversibly. Answering this question is fundamental to understand of the oceanic equilibration and to improve our ability to simulate/predict the climate. In this study, we combine the ocean surface drifter measurements and satellite altimeter data and detect a counterintuitive feature of energy level of submesoscale motions (1–50 km) through the life cycle of mesoscale eddies. The submesoscale energy level is low during mature phase when eddies are strong, and high in formation/decaying phases when eddies are weak. Further investigations reveal that the submesoscale energy level depends positively on the deformation strain rate around the mesoscale eddies. This latter fact points to the potential importance of mesoscale deformation field in controlling the energy transfer between the mesoscale and submesoscale motions.

1. Introduction

The oceanic general circulation is forced externally by fluxes of momentum, heat, water, and other materials at the sea surface, with O(1,000 km) or larger scales. Climate equilibrium is necessarily achieved by balancing this input energy through dissipation at very small scale around centimeters, where molecular diffusion is important and effective. A dynamical route to dissipation that traverses all the intervening scales is thus needed to close the whole energy budget, which in return will shape the global oceanic equilibrium state. Mesoscale eddies with horizontal scale of tens to hundreds of kilometers are well known to be the dominant reservoir of kinetic energy of the world ocean (Ferrari & Wunsch, 2009). They are ubiquitous in existence and, to a lowest order, in geostrophic balance due to the Earth rotation. The mesoscale eddies serve as a principal sink for the energy of planetary-scale mean oceanic circulation through *balanced* instabilities, for example, the quasi-geostrophic barotropic and baroclinic instabilities (Vallis, 2006) and, by so doing, they play a critical role within the route to dissipation. On the other hand, the balanced mesoscale eddies are characterized by inverse energy cascade (Charney, 1971) that transfers energy back to larger-scale motions and cannot provide an effective energy route to smaller scales. The key issue here is how the balanced mesoscale flows break the constraint of geostrophic balance and

transfer energy to smaller scales (Qiu et al., 2017, 2018). This is where the submesoscale ageostrophic motions can play a central role.

The approximate scale range for submesoscale flow is 1–50 km in the horizontal and 1–10 days in time, for which the geostrophic balance can no longer be held, resulting in substantial ageostrophic motions and allowing forward energy cascade to smaller scales (Capet et al., 2008; McWilliams, 2016). The submesoscale ageostrophic motions cover a wide range of dynamical processes: They include ageostrophic wave motions, such as near inertial waves and internal gravity waves, and nonwave motions, such as the ageostrophic submesoscale vortices and filaments, and the Ekman flow by air-sea interactions (Chelton, 2013; Gaube et al., 2015; Renault et al., 2016). Arising from processes like wave-current interactions and submesoscale instabilities, such as frontogenesis (Hoskins, 1982; Hoskins & Bretherton, 1972), mixed-layer instability (Colas et al., 2013; Fox-Kemper et al., 2008), symmetric instability (Haine & Marshall, 1998; Thomas et al., 2013), or anticyclonic-ageostrophic instability (McWilliams, 2008; McWilliams & Yavneh, 1998; Molemaker et al., 2005), submesoscale ageostrophic motions are dynamically important because they determine the equilibrium state through releasing of available energy contained within the mesoscale balanced motions. Additionally, the submesoscale processes are also crucial to how the surface ocean communicates with the subsurface interior ocean, affecting the mixed layer development and upper-ocean thermal anomalies, and achieving efficient exchanges with the permanent thermocline (Boccaletti et al., 2007; Callies et al., 2015; Fox-Kemper et al., 2008; Klein et al., 2008; Lapeyre et al., 2006; Sasaki et al., 2014).

Despite the crucial importance of the submesoscale processes, their relatively short spatiotemporal scales present an observational barrier that delayed a comprehensive dynamical understanding. Moored arrays and ship surveys are typically too expensive to provide the spatial sampling needed for synoptic observations at these scales. As one of the most important satellite remote sensing methods, the currently operating altimeters miss the submesoscale footprint because of the 100- to 300-km spacing between the satellite ground tracks. Difficulties associated with the simultaneous measurement of submesoscale features can be circumvented by Lagrangianly based observations. The Global Positioning System tracked surface drifters nowadays have large enough numbers to achieve a global coverage and can provide accurate real-time position time series (Lumpkin, 2016; Lumpkin et al., 2016; Ohlmann et al., 2017; Poje et al., 2017). With a typical sampling interval at about 6 hr, the drifters are able to resolve the submesoscale velocity signals at the sea surface globally. It is worth emphasizing that the submesoscale signals captured by drifters contain not only the ageostrophic wave motions but also the submesoscale nonwave motions. While a significant portion of the drifter-measured signals represent near inertia and internal gravity waves (Elipot et al., 2010), submesoscale fronts and eddies can also be quantitatively observed by the surface drifters (Ohlmann et al., 2017).

Mesoscale eddies, on the other hand, can be identified and tracked by sequential maps of altimeter-measured sea surface height (SSH) anomaly (SSHA) and the detailed information of eddy's life cycle is readily accessible (Chelton et al., 2011; Samelson et al., 2014). Since the energy level of mesoscale eddies experiences substantial variations during different phases of their life cycle and the submesoscale motions are expected to depend on the evolution of the mesoscale eddies, we now have a unique opportunity to explore the connection between the submesoscale ageostrophic energy level and the variation of mesoscale geostrophic eddies based on observational data. The main focus of this paper is to investigate this connection by combining global-coverage drifter measurements and the altimeter-tracked mesoscale eddies data sets. Here we show that the submesoscale ageostrophic kinetic energy exhibits an unexpected evolution through the eddy life cycle. In addition, the energy level of submesoscale ageostrophic motions is found to depend positively on the local mesoscale deformation strain rate: The stronger the deformation flow field, the higher the ageostrophic kinetic energy level.

2. Data and Methods

2.1. Altimetry and Eddy Tracking Data Set

The delay time altimetry product provided by Archiving Validation and Interpretation of Satellite Oceanographic data (AVISO) Version 3 is used here. This multiple-satellite-merged data set contains the global gridded SSH, SSHA, and sea surface geostrophic velocity anomaly (u_g, v_g) data with a (¼)° resolution for every 7 days from October 1992 to April 2012. Based on the altimetry data set, a 19.5-year eddy identification and tracking data set is provided by automatic eddy identification and tracking algorithm (Chelton et al.,

2011). This eddy identification and tracking data set provides the longitude, latitude, time, eddy radius R_0, and polarity information of a total of 215,184 eddy observations in the global ocean.

2.2. Surface Drifter Data

The surface drifter data used here is provided by the Drifter Data Assembly Center of National Oceanic and Atmospheric Administration. The Drifter Data Assembly Center assembles and provides uniform quality control of surface velocity data by satellite-tracked surface drifting buoy observations. The surface velocity measurements are provided for every 6 hr from year 1993 to 2011 and have a global coverage containing a total of 22,249,337 observational data points (see supporting information).

2.3. Geostrophic Kinetic Energy and Strain

The eddy surface geostrophic kinetic energy is computed as $E_g(t) = V_g^2/2$, where V_g is the averaged geostrophic speed observed by altimeter within a ring-shaped area around the eddy. In order to take eddy's deformation into account, this ring-shaped area is enclosed by two closed SSHA contours around the eddy center: η_{R05} and η_{R15}, where η_{R05} (η_{R15}) denotes the averaged SSHA value along the circle with a radius $0.5\times R_0$ ($1.5\times R_0$) around the eddy center. For an eddy with life span T_e, the time t starts from its formation moment can be normalized by T_e to get the normalized time $t_n = t/T_e$, where $t_n = 0$ at the eddy formation moment and $t_n = 1$ at its ending moment. The eddy's energy can be averaged within the period of $0.3 < t_n < 0.7$ to get its mature-phase average energy E_{ave}, which is a constant for an individual eddy. The eddy energy time series can be normalized as $E_{gn}(t_n) = E_g(t/T_e)/E_{ave}$. In order to composite the normalized kinetic energy curve through the eddy life cycle, the normalized eddy kinetic energy is averaged over t_n for all available eddies identified by the tracking algorithm. All errors in this study are estimated by the standard error of the mean value as $Std/N^{1/2}$, where Std and N are the standard deviation and data number used to compute the average, respectively.

The geostrophic strain rate S_g is computed using the surface geostrophic velocity anomaly (u_g, v_g) from the altimeter data:

$$S_g = \sqrt{\left(\frac{\partial u_g}{\partial x} - \frac{\partial v_g}{\partial y}\right)^2 + \left(\frac{\partial v_g}{\partial x} + \frac{\partial u_g}{\partial y}\right)^2}. \quad (1)$$

For each eddy, the strain rate time series $S_g(t)$ is also computed by averaging within the ring-shaped area around the eddy center. Similar to the eddy kinetic energy, the strain rate is also normalized by the mature-phase average energy $S_n(t_n) = S_g(t/T_e)/E_{ave}$ and its composition is obtained by averaging over t_n for all available eddies.

2.4. Ageostrophic Kinetic Energy

The drifters observe the absolute horizontal velocity $\vec{u}$ at the ocean surface (Lumpkin, 2016; Lumpkin et al., 2016; Ohlmann et al., 2017; Poje et al., 2017). The focus of this study is to investigate the submesoscale ageostrophic motions associated with the mesoscale eddies, for example, the inertial gravity waves or the nonwave submesoscale filaments. In order to extract the signals of the ageostrophic motions, we define the ageostrophic velocity as $\vec{u}_a = \vec{u} - \vec{u}_g - \vec{u}_0$, where $\vec{u}_g$ is the simultaneous geostrophic velocity at the drifter location estimated from the altimeter data, and $\vec{u}_0$ is the climatological mean surface velocity computed from the drifter absolute velocity $\vec{u}$. Although the geostrophic velocity used here will introduce errors from altimeter observations, this will not change the results of this study fundamentally (see discussion in section 3.2). Considering that the ageostrophic velocity component of the mesoscale eddies in gradient-wind balance, or by cyclogeostrophic effect (Penven et al., 2014), can also be contained in $\vec{u}_a$, a high-pass filter is used to eliminate this balanced ageostrophic component in $\vec{u}_a$. Constrained by the Lagrangian drifter observation, only temporal filter rather than temporal-spatial filter (Lu et al., 2016) can be used. As the typical time scale of the oceanic submesoscale processes is about 1–10 days, the cutoff period of our high-pass filter is set to 7 days, which is longer than most of the unbalanced submesoscale ageostrophic motions and, at the same time, substantially shorter than the typical evolution time scale of mesoscale eddies (see supporting information Text S3 for sensitivity of this cutoff period). By applying the high-pass filter to $\vec{u}_a$, the high-pass-filtered ageostrophic velocity $\vec{u}_{HP}$ is obtained that we consider representing the unbalanced submesoscale

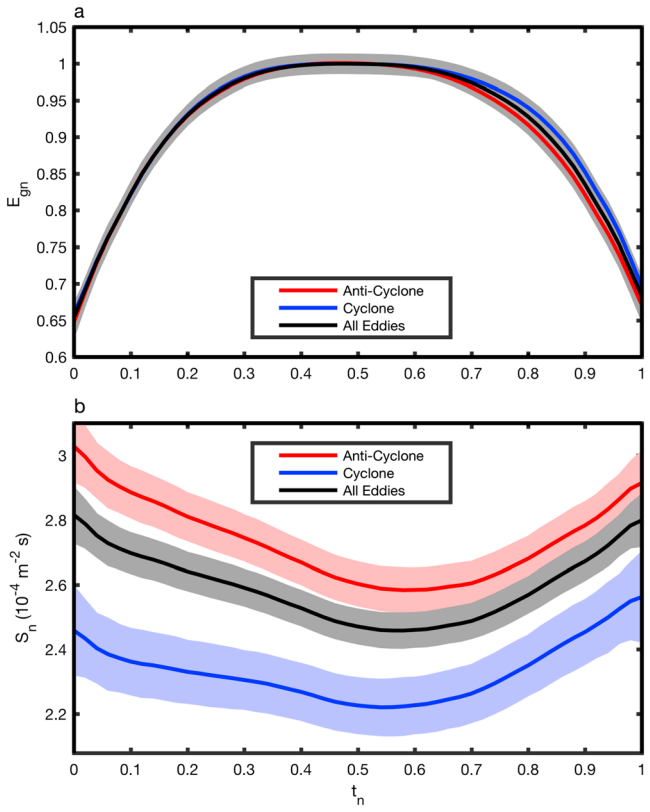

Figure 1. Temporal evolution of eddy kinetic energy and strain rate. (a) Composited curves of normalized surface eddy kinetic energy as a function of eddy life cycle. The vertical coordinate is normalized geostrophic kinetic energy level and the horizontal coordinate is the normalized time of eddy life cycle t_n. For each eddy, its surface eddy kinetic energy $E_g(t)$ is normalized by its average value in eddy's mature phase ($0.3 < t_n < 0.7$) to get the normalized time series E_{gn} (t_n). The black curve represents the result averaged of all eddies, and the red and blue curves for anticyclonic and cyclonic eddies, respectively. The light gray shadings represent the envelope of the error bars of all three curves. (b) Composited curves of normalized strain rate S_n as a function of eddy life cycle. The vertical coordinate is normalized geostrophic strain rate S_n, and the horizontal coordinate is still t_n. The strain rate is also normalized by averaged eddy kinetic energy in mature phase. The unit for S_n is m^{-2}·s. The black curve represents the result averaged of all eddies, and the red and blue curves for anticyclonic and cyclonic eddies, respectively. The light-colored shadings represent the error bars of each curve.

ageostrophic motions. The residual velocity $\vec{u}_{LP} = \vec{u}_a - \vec{u}_{HP}$ can be treated as the low-pass-filtered ageostrophic velocity, containing the mesoscale eddy's ageostrophic components in gradient-wind balance (see supporting information).

The total, high-pass and low-pass ageostrophic kinetic energy values are defined as $E_a = u_a^2/2$, $E_{HP} = u_{HP}^2/2$ and $E_{LP} = u_{LP}^2/2$, respectively. The global gridded mean values and standard deviations of the absolute, high-pass and low-pass ageostrophic kinetic energy are calculated with a 2° average window: E_{a0}/E_{astd}, E_{HP0}/E_{HPstd} and E_{LP0}/E_{LPstd}. In order to remove the influence of regional differences in the ageostrophic kinetic energy, the time series are standardized with their local mean and standard deviations: $E_{as} = (E_a - E_{a0})/E_{astd}$, $E_{HPs} = (E_{HP} - E_{HP0})/E_{HPstd}$ and $E_{LPs} = (E_{LP} - E_{LP0})/E_{LPstd}$. In order to composite the horizontal distribution of ageostrophic kinetic energy around mesoscale eddies, the drifter location is projected onto an eddy-centered coordinate first. Specifically, if the horizontal location of a given drifter is (x, y), and if the location of its nearest simultaneous eddy center is (x_c, y_c), the normalized projected drifter location is given by (x_n, y_n), where $x_n = (x - x_c)/R_0$ and $y_n = (y - y_c)/R_0$. Using the normalized eddy center coordinate, the standardized absolute, high-pass and low-pass ageostrophic kinetic energy are then composited to evaluate $E_{as}(x_n, y_n)$, E_{HPs} (x_n, y_n) and E_{LPs} (x_n, y_n). To compute the temporal evolution of ageostrophic energy around mesoscale eddies, we first select all available drifter data within the ring-shaped area around the eddy center. Take the high-pass-filtered ageostrophic kinetic energy $E_{HP}(t)$, for example, similar to the eddy geostrophic energy and strain rate, the ageostrophic energy is normalized by the mature-phase average geostrophic energy of the mesoscale eddy E_{HPn} $(t_n) = E_{HP}$ $(t/T_e)/E_{ave}$. The composited evolution of the high-pass ageostrophic energy through the eddy life cycle is finally obtained by averaging E_{HPn} over t_n.

3. Results

3.1. Geostrophic Energy and Strain Evolution

Evolution of eddy kinetic energy level through its life circle can be obtained by using only the altimetry data. While individual eddies can change their energy level significantly on time scales of weeks even during their mature phases, consistent features of their energy evolution can emerge when a large number of eddies are composited, including the constant energy level during eddy's mature phase (Samelson et al., 2014). By compositing the normalized kinetic energy E_{gn} (t_n) of all eddies, the black curve in Figure 1a shows the evolution of geostrophic kinetic energy level of the mesoscale eddies: The eddy kinetic energy experiences a fast increase in the formation phase ($t_n < 0.3$), remains at a relatively stable high level in the mature phase ($0.3 < t_n < 0.7$), and drops rapidly in the final decaying phase ($t_n > 0.7$). The blue and red curves in Figure 1a show E_{gn} (t_n) for the cyclonic and anticyclonic eddies, respectively. These two curves overlap with each other, indicating the features of kinetic energy evolution through the eddy life cycle are not sensitive to the eddy polarity.

Submesoscale processes can arise dynamically through nonlinear interactions between mesoscale eddies, and its key characteristic is the ageostrophic component in the flow field. In order to break the constraint of geostrophic balance, the strain rate of the mesoscale geostrophic flow field could play a central role. In particular, the geostrophic strain field acts to continuously squeeze the fluid in one direction and stretch it in the perpendicular direction. When the scale along the squeezing direction become small enough and the geostrophic balance can no longer be held, submesoscale ageostrophic motions emerge (Thomas, 2012). Thus, large strain rate of the geostrophic stirring field favors the development of submesoscale perturbations in

various instability theories (Capet et al., 2008; Hoskins, 1982; Hoskins & Bretherton, 1972; McWilliams, 2008, 2016; McWilliams & Yavneh, 1998; Molemaker et al., 2005). Since the strong strain rate is expected to be located around the eddy edges where the strongest interactions between eddies occur, only the strain rate within the ring-shaped area around the eddy center is taken into account in our analysis.

The normalized strain rate S_n (t_n) through the eddy life cycle is shown in Figure 1b. It exhibits a striking feature: The strain rate is large in the formation and decaying phases of the eddies and weak in the mature phase. From a physical perspective, the mesoscale eddy tends to be more stable in its mature phase and can resist deformation induced by nearby eddies and background currents; hence, the strain rate in the mature phase can be expected to be relatively small when compared to the formation/decaying phases. Another important feature revealed in Figure 1b is that the strain rate of the anticyclonic eddies is larger than that of the cyclonic eddies. One possible explanation for this is that the anticyclonic eddies have a tendency to break down more easily than cyclonic eddies partly due to the symmetric instability (Haine & Marshall, 1998; Thomas et al., 2013) or anticyclonic-ageostrophic instability (McWilliams & Yavneh, 1998). The anticyclonic eddies are thus more vulnerable to deformation and the strain rate is likely to be larger for anticyclonic than cyclonic eddies. Given that the larger strain rate favors the development of submesoscale perturbations, it is expected that the submesoscale ageostrophic energy level will be higher in the formation/decaying phase than the mature phase of mesoscale eddies and that the anticyclonic eddies may have stronger submesoscale ageostrophic motions than the cyclonic eddies. This is indeed the case as shown in following section.

3.2. Ageostrophic Energy Distributions and Evolution

If the submesoscale ageostrophic energy has a dynamical connection with mesoscale eddies, distinguishable horizontal distribution patterns of the ageostrophic energy are expected within the eddy-occupied areas. Figures 2a to 2c show the distributions of the composite total, high-pass- and low-pass-filtered ageostrophic kinetic energy in the eddy center coordinates. An obvious feature of the distributions is that the high ageostrophic energy band is located within a ring-shaped area around the eddy, where the strain rate is expected to be large. It is noticeable that the high-pass-filtered ageostrophic kinetic energy E_{HPs} (Figure 2b) has almost the same horizontal distribution as the total energy E_{as} (Figure 2a). Additionally, the amplitude of the nonstandardized high-pass kinetic energy is several times larger than the low-pass-filtered kinetic energy (not shown). This means that the major part of the total ageostrophic energy E_a is given by the high-pass component E_{HP}. These results are not sensitive to the polarity of eddies (see supporting information). Considering that the E_{HP} represents the energy level of unbalanced submesoscale ageostrophic motions, we will focus on E_{HP} in following analysis.

Figure 2d shows the temporal evolution of the normalized, high-pass ageostrophic energy E_{HPn} through the eddy life cycle for all eddies and cyclonic versus anticyclonic eddies. The composite E_{HPn} level tends to be higher in the formation/decaying phases than the mature phase of mesoscale eddies, and the anticyclonic eddies have stronger submesoscale ageostrophic energy than the cyclonic eddies, which can be expected from the strain rate evolution through the eddy life cycle (recall Figure 1b). It is worth noting that since the energy level of the ageostrophic motions is relatively small in eddy's mature phase when the error of the geostrophic velocities can be expected to be the largest, it implies that the composite results shown in Figure 2d are not due to the altimetry errors.

The results here cannot be explained by the enhancement of near inertial waves in anticyclones (Elipot et al., 2010; Kunze, 1985) or the mixed-layer instability. In contrast, the frontogenesis and anticyclonic-ageostrophic instability all suggest possible connection between the geostrophic strain field and the ageostrophic kinetic energy level, which is hinted by the combined result of Figures 1b and 2d. Although identifying the responsible instability theory is beyond the scope of this paper, the quantitative connection between the geostrophic strain field and the ageostrophic kinetic energy level around mesoscale eddies can be assessed purely by observational data. In order to investigate this connection, only the data point within the eddy-edge ring-shaped area is taken into account. The curve in Figure 2e shows a clear tendency for the submesoscale ageostrophic kinetic energy to increase monotonously with the geostrophic strain rate. There is a possibility that the ageostrophic kinetic energy and the geostrophic strain rate could both be larger around stronger mesoscale eddies, and it is the increased amplitude of the mesoscale eddies that causes the

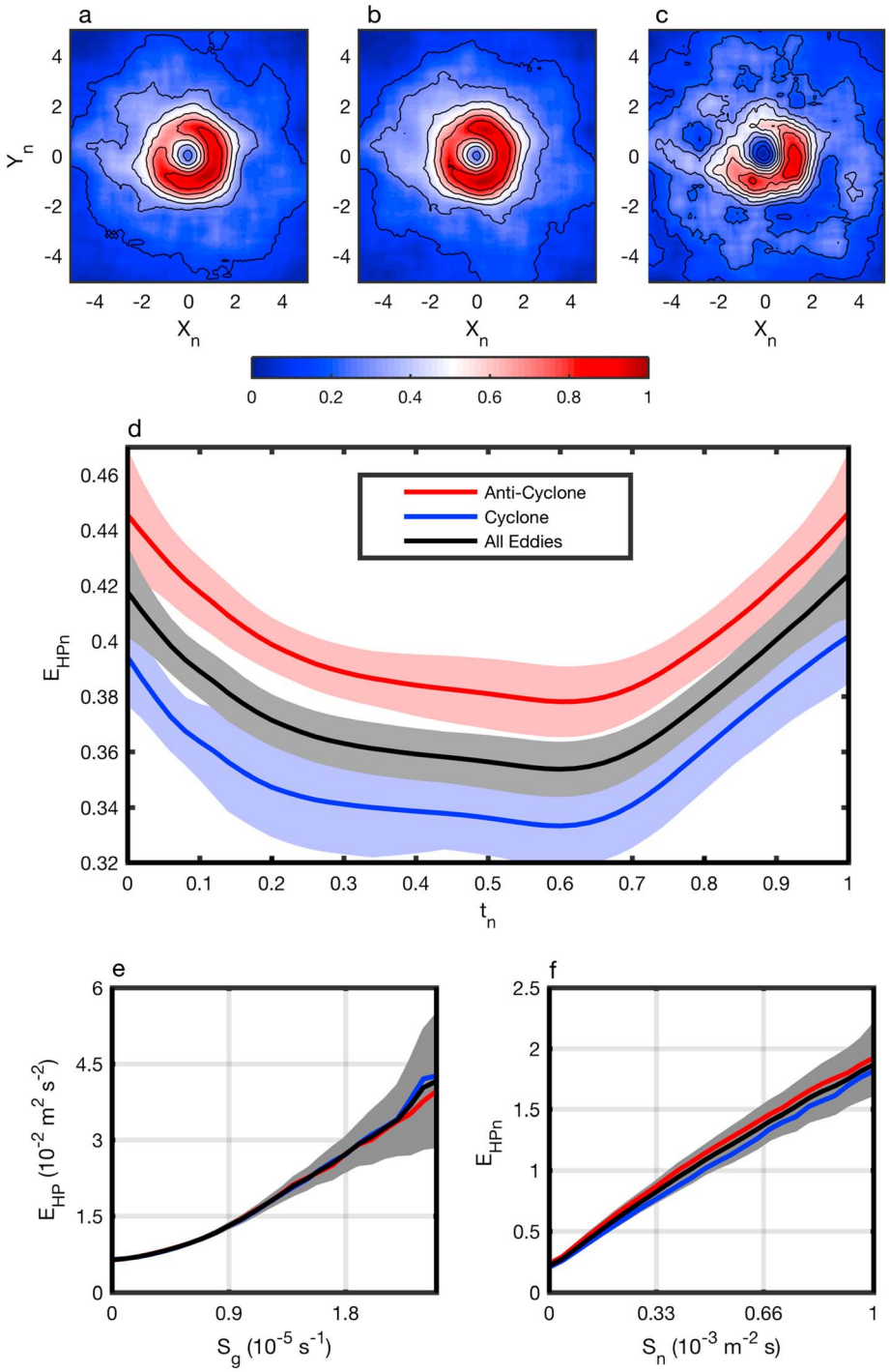

Figure 2. Spatial and temporal variation of ageostrophic kinetic energy. Distribution of the standardized (a) total ageostrophic kinetic energy E_{as} (x_n, y_n), (b) high-pass ageostrophic kinetic energy E_{HPs} (x_n, y_n), and (c) low-pass ageostrophic kinetic energy E_{LPs} (x_n, y_n) composited in the normalized eddy center coordinate (x_n, y_n) for all available eddies. All the standardized ageostrophic kinetic energy time series are computed from the drifter data, and then projected onto the eddy center coordinate. (d) Temporal evolution of ageostrophic kinetic energy through eddy life cycle. The vertical coordinate is normalized high-pass ageostrophic kinetic energy, and the horizontal coordinate is the normalized time relative to the eddy formation moment t_n. The black line represents the result for all eddies. The red and blue curves for the anticyclonic and cyclonic eddy, respectively. The light-colored shadings represent the error bars of each curve. The high-pass ageostrophic kinetic energy is normalized by averaged eddy kinetic energy in its mature phase. (e) Curve of high-pass-filtered ageostrophic kinetic energy E_{HP} changing with the geostrophic strain rate S_g. The red, blue, and black curves represent the averaged value of E_{HP} for anticyclonic, cyclonic, and all eddies, respectively. The gray range represents the envelope of their error bars. (f) Curves of normalized high-pass-filtered ageostrophic kinetic energy E_{HPn} changing with the normalized geostrophic strain rate S_n. Both of them are normalized by simultaneous nearest eddy mature-phase averaged kinetic energy. Both curves are averaged for available drifter data within the ring-shaped area around eddy.

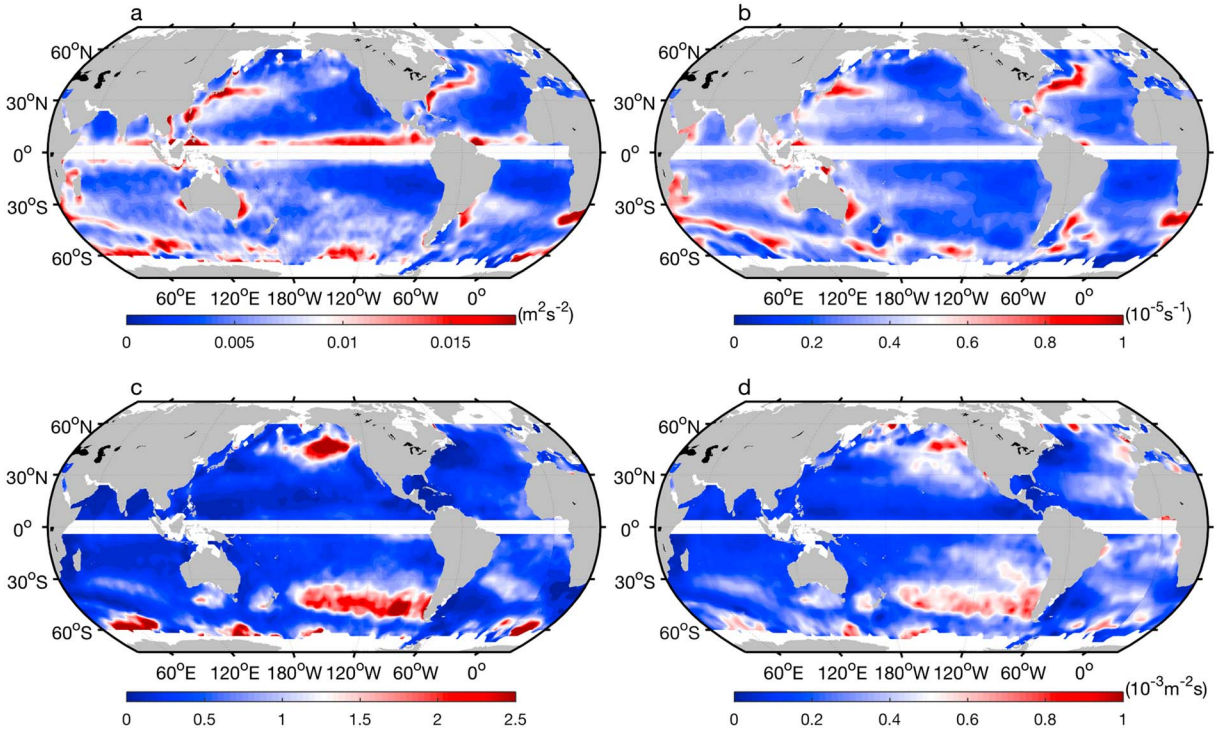

Figure 3. Global distributions of ageostrophic energy and geostrophic strain rate. (a) The high-pass ageostrophic kinetic energy E_{HP}, unit: m^2/s^2. (b) The geostrophic strain rate S_g, unit: s^{-1}. (c) The normalized high-pass ageostrophic kinetic energy E_{HPn}, which is nondimensional. (d) The normalized geostrophic strain rate S_n, unit m^{-2}·s. These parameters are averaged on a 2° × 2° global grid with a 4° × 4° moving average window by using all available drifter and altimetry data.

increasing trend in Figure 2e. In order to rule out this possibility, we normalize both the ageostrophic energy and geostrophic strain rate by the eddy mature-phase averaged energy. The normalized curve shown in Figure 2f reveals that the normalized submesoscale ageostrophic kinetic energy also increases monotonously with the normalized geostrophic strain rate. This suggests that irrespective of the strength of a mesoscale eddy, a stronger geostrophic strain is likely to accompany with a higher energy level of submesoscale ageostrophic motions. These results are not sensitive to the polarity of eddies, as shown in Figures 2e and 2f.

4. Summary and Discussion

From a traditional point of view, when instabilities cause an energy transfer from mesoscale eddies to submesoscale motions, the decaying of mesoscale eddies will be accompanied by an enhanced ageostrophic kinetic energy. Thus, it is expected that the submesoscale ageostrophic energy is intensified during eddy's decaying phase as shown in Figure 2d. The unexpected result is that the submesoscale ageostrophic energy is also intensified during the formation phase of eddies, indicating that an effective increase of submesoscale ageostrophic energy occurs not necessarily at the expense of decaying mesoscale eddies. Our results here suggest that when mesoscale eddies are vulnerable to external deformation and exhibit larger energy variations in their formation/decaying phases, the conditions become favorable for higher energy level of submesoscale ageostrophic motions.

The geostrophic eddies are relatively strong in regions where the energetic larger-scale currents are unstable. On one hand, the high geostrophic energy level within these regions provides energy sources for development of submesoscale ageostrophic motions. On the other hand, these regions are characterized by energetic background currents and abundant mesoscale eddies, and the regional eddy-eddy and eddy-mean flow interactions are expected to be similarly vigorous. The resulted strong geostrophic strain rate within these regions, as shown in Figure 3b, can provide favorable conditions inductive for the high-energy-level submesoscale motions. With sufficient energy sources and favorable conditions, the ageostrophic energy

level within these regions is also high as shown in Figure 3a. Although there is a general consistence between the global distributions of the ageostrophic kinetic energy and the geostrophic strain rate, there exist also visible exceptions, for example, a high ageostrophic energy level, but with low strain rate, appears in the eastern tropical Pacific, which emerge from the tropical instability waves (Qiao & Weisberg, 1995). These exceptions indicate that the strain rate may not be the only factor determining the ageostrophic energy level, and more comprehensive investigations are called for in future studies.

The ageostrophic energy level Figure 3a is relatively high in two particular regions, the northeast corner of the North Pacific and the southeast corner of the South Pacific, where the energy level of mesoscale eddies reaches the global minimum. The northeast corner of the North Pacific is even known as the *eddy desert* (Chelton et al., 2007). As shown in Figure 3c, the global distribution of the normalized ageostrophic energy E_{HPn} exhibits two high-value centers located just at the northeast corner of the North Pacific and the southeast corner of the South Pacific. This means that the conditions within these regions are favorable for high submesoscale ageostrophic energy level. From the results of Figure 2f, it is expected that the strain rate should also be relatively large as compared to the local geostrophic eddy energy level within these two particular regions. In order to test this hypothesis, we show in Figure 3d the distribution of the normalized strain rate S_n and the two regions exhibit high-value centers. This result indicates that the existence of strong eddies may not be an inductive condition for strong submesoscale ageostrophic motions; in contrast, it is the large strain field that serves as the key element for enhanced submesoscale ageostrophic motions, especially in where the background geostrophic energy level is relatively low.

Our present results do not provide comprehensive answers to what determines the forward energy cascade to submesoscale ageostrophic motions. Instead, by focusing on the ageostrophic energy variations through the eddy life cycle and by establishing the connection between the ageostrophic energy and geostrophic strain field, we hope to motivate future studies to gain a better dynamical understanding of the energy balance of the ocean circulation system, especially when the next-generation Surface Water Ocean Topography satellite mission can provide simultaneous observations of mesoscale eddies and submesoscale signals with a horizontal resolution down to ~15 km (Fu & Ferrari, 2008; Morrow & Fu, 2011; Rogé et al., 2017). Additionally, the results here also provide an observational baseline for the eddy-resolving climate models to test whether they correctly simulate the forward energy cascade from mesoscale eddies to submesoscale ageostrophic motions, especially through the different phases of eddy life cycle.

Acknowledgments
The authors declare no competing financial interests. The AVISO altimeter data are downloaded from the website: https://www.aviso.altimetry.fr/en/data/products/sea-surface-height-products/global/index.html#c5123. The mesoscale eddy identification and tracking data set is downloaded from the website: http://cioss.coas.oregonstate.edu/eddies. The surface drifter data set is from the website: ftp://ftp.aoml.noaa.gov/phod/pub/buoydata. This research was supported by the National Natural Science Foundation of China under Grants 41506007 and 41876001 and the National Programme on Global Change and Air-Sea Interaction under Grant GASI-IPOVAI-04.

References

Boccaletti, G., Ferrari, R., & Fox-Kemper, B. (2007). Mixed layer instabilities and restratification. *Journal of Physical Oceanography*, *37*(9), 2228–2250. https://doi.org/10.1175/JPO3101.1

Callies, J., Ferrari, R., Klymak, J. M., & Gula, J. (2015). Seasonality in submesoscale turbulence. *Nature Communications*, *6*(1), 6862. https://doi.org/10.1038/ncomms7862

Capet, X., McWilliams, J. C., Molemaker, M. J., & Shchepetkin, A. J. (2008). Mesoscale to submesoscale transition in the California current system. Part I: Flow structure, eddy flux, and observational tests. *Journal of Physical Oceanography*, *38*(1), 29–43. https://doi.org/10.1175/2007JPO3671.1

Charney, J. G. (1971). Geostrophic turbulence. *Journal of the Atmospheric Sciences*, *28*(6), 1087–1095. https://doi.org/10.1175/1520-0469(1971)028<1087:GT>2.0.CO;2

Chelton, D. B. (2013). Ocean-atmosphere coupling: Mesoscale eddy effects. *Nature Geoscience*, *6*(8), 594–595. https://doi.org/10.1038/ngeo1906

Chelton, D. B., Schlax, M. G., & Samelson, R. M. (2011). Global observations of nonlinear mesoscale eddies. *Progress in Oceanography*, *91*(2), 167–216. https://doi.org/10.1016/j.pocean.2011.01.002

Chelton, D. B., Schlax, M. G., Samelson, R. M., & de Szoeke, R. A. (2007). Global observations of large oceanic eddies. *Geophysical Research Letters*, *34*, L15606. https://doi.org/10.1029/2007GL030812

Colas, F., Capet, X., McWilliams, J. C., & Li, Z. (2013). Mesoscale eddy buoyancy flux and eddy-induced circulation in eastern-boundary currents. *Journal of Physical Oceanography*, *43*(6), 1073–1095. https://doi.org/10.1175/JPO-D-11-0241.1

Elipot, S., Lumpkin, R., & Prieto, G. (2010). Modification of inertial oscillations by the mesoscale eddy field. *Journal of Geophysical Research*, *115*, C09010. https://doi.org/10.1029/2009JC005679

Ferrari, R., & Wunsch, C. (2009). Ocean circulation kinetic energy—Reservoirs, sources, and sinks. *Annual Review of Fluid Mechanics*, *41*(1), 253–282. https://doi.org/10.1146/annurev.fluid.40.111406.102139

Fox-Kemper, B., Ferrari, R., & Hallberg, R. W. (2008). Parameterization of mixed layer eddies. I. Theory and diagnosis. *Journal of Physical Oceanography*, *38*(6), 1145–1165. https://doi.org/10.1175/2007JPO3792.1

Fu, L.-L., & Ferrari, R. (2008). Observing oceanic submesoscale processes from space. *Eos, Transactions American Geosphysical Union*, *89*(48), 488–488. https://doi.org/10.1029/2008EO480003

Gaube, P., Chelton, D. B., Samelson, R. M., Schlax, M. G., & O'Neill, L. W. (2015). Satellite observations of mesoscale eddy-induced Ekman pumping. *Journal of Physical Oceanography*, *45*(1), 104–132. https://doi.org/10.1175/JPO-D-14-0032.1

Haine, T., & Marshall, J. C. (1998). Gravitational, symmetric, and baroclinic instability of the ocean mixed layer. *Journal of Physical Oceanography*, *28*(4), 634–658. https://doi.org/10.1175/1520-0485(1998)028<0634:GSABIO>2.0.CO;2

Hoskins, B. J. (1982). The mathematical theory of frontogenesis. *Annual Review of Fluid Mechanics*, *82*, 131–151.

Hoskins, B. J., & Bretherton, F. P. (1972). Atmospheric frontogenesis models: Mathematical formulation and solution. *Journal of the Atmospheric Sciences*, *29*(1), 11–37. https://doi.org/10.1175/1520-0469(1972)029<0011:AFMMFA>2.0.CO;2

Klein, P., Hua, B. L., Lapeyre, G., Capet, X., le Gentil, S., & Sasaki, H. (2008). Upper ocean turbulence from high-resolution 3D simulations. *Journal of Physical Oceanography*, *38*(8), 1748–1763. https://doi.org/10.1175/2007JPO3773.1

Kunze, E. (1985). Near-inertial wave propagation in geostrophic shear. *Journal of Physical Oceanography*, *15*(5), 544–565. https://doi.org/10.1175/1520-0485(1985)015<0544:NIWPIG>2.0.CO;2

Lapeyre, G., Klein, P., & Hua, B. L. (2006). Oceanic restratification forced by surface frontogenesis. *Journal of Physical Oceanography*, *36*(8), 1577–1590. https://doi.org/10.1175/JPO2923.1

Lu, J., Wang, F., Liu, H., & Lin, P. (2016). Stationary mesoscale eddies, upgradient eddy fluxes, and the anisotropy of eddy diffusivity. *Geophysical Research Letters*, *43*, 743–751. https://doi.org/10.1002/2015GL067384

Lumpkin, R. (2016). Global characteristics of coherent vortices from surface drifter trajectories. *Journal of Geophysical Research: Oceans*, *121*, 1306–1321. https://doi.org/10.1002/2015JC011435

Lumpkin, R., Centurioni, L., & Perez, R. C. (2016). Fulfilling observing system implementation requirements with the global drifter array. *Journal of Atmospheric and Oceanic Technology*, *33*(4), 685–695. https://doi.org/10.1175/JTECH-D-15-0255.1

McWilliams, J. C. (2008). Fluid dynamics at the margin of rotational control. *Environmental Fluid Mechanics*, *8*(5-6), 441–449. https://doi.org/10.1007/s10652-008-9081-8

McWilliams, J. C. (2016). Submesoscale currents in the ocean. *Proceedings of the Royal Society of London A*, *472*(2189), 20160117. https://doi.org/10.1098/rspa.2016.0117

McWilliams, J. C., & Yavneh, I. (1998). Fluctuation growth and instability associated with a singularity of the balance equations. *Physics of Fluids*, *10*(10), 2587–2596. https://doi.org/10.1063/1.869772

Molemaker, M. J., McWilliams, J. C., & Yavneh, I. (2005). Baroclinic instability and loss of balance. *Journal of Physical Oceanography*, *35*(9), 1505–1517. https://doi.org/10.1175/JPO2770.1

Morrow, R., & Fu, L.-L. (2011). Observing mesoscale to submesoscale dynamics today, and in the future with SWOT. *IEEE International Geoscience and Remote Sensing Symposium*, *89*, 2689–2691. https://doi.org/10.1109/IGARSS.2011.6049757

Ohlmann, J. C., Molemaker, M. J., Baschek, B., Holt, B., Marmorino, G., & Smith, G. (2017). Drifter observations of submesoscale flow kinematics in the coastal ocean. *Geophysical Research Letters*, *44*, 330–337. https://doi.org/10.1002/2016GL071537

Penven, P., Halo, I., Pous, S., & Marie, L. (2014). Cyclogeostrophic balance in the Mozambique Channel. *Journal of Geophysical Research: Oceans*, *119*, 1054–1067. https://doi.org/10.1002/2013JC009528

Poje, A. C., Özgökmen, T. M., Bogucki, D. J., & Kirwan, A. D. Jr. (2017). Evidence of a forward energy cascade and Kolmogorov self-similarity in submesoscale ocean surface drifter observations. *Physics of Fluids*, *29*(2), 020701. https://doi.org/10.1063/1.4974331

Qiao, L., & Weisberg, R. H. (1995). Tropical instability wave kinematics: Observations from Tropical Instability Wave Experiment (TIWE). *Journal of Geophysical Research*, *100*(C5), 8677–8693. https://doi.org/10.1029/95JC00305

Qiu, B., Chen, S., Klein, P., Wang, J., Torres, H., Fu, L. L., & Menemenlis, D. (2018). Seasonality in transition scale from balanced to unbalanced motions in the World Ocean. *Journal of Physical Oceanography*, *48*(3), 591–605. https://doi.org/10.1175/JPO-D-17-0169.1

Qiu, B., Nakano, T., Chen, S., & Klein, P. (2017). Submesoscale transition from geostrophic flows to internal waves in the northwestern Pacific upper ocean. *Nature Communications*, *8*, 14055. https://doi.org/10.1038/ncomms14055

Renault, L., Molemaker, M. J., McWilliams, J. C., Shchepetkin, A. F., Lemarié, F., Chelton, D., et al. (2016). Modulation of wind work by oceanic current interaction with the atmosphere. *Journal of Physical Oceanography*, *46*(6), 1685–1704. https://doi.org/10.1175/JPO-D-15-0232.1

Rogé, M., Morrow, R., Ubelmann, C., & Gerald, D. (2017). Using a dynamical advection to reconstruct a part of the SSH evolution in the context of SWOT, application to the Mediterranean Sea. *Ocean Dynamics*, *67*(8), 1047–1066. https://doi.org/10.1007/s10236-017-1073-0

Samelson, R. M., Schlax, M. G., & Chelton, D. B. (2014). Randomness, symmetry, and scaling of mesoscale eddy life cycles. *Journal of Physical Oceanography*, *44*(3), 1012–1029. https://doi.org/10.1175/JPO-D-13-0161.1

Sasaki, H., Klein, P., Qiu, B., & Sasai, Y. (2014). Impact of oceanic-scale interactions on the seasonal modulation of ocean dynamics by the atmosphere. *Nature Communications*, *5*(1), 5636. https://doi.org/10.1038/ncomms6636

Thomas, L. N. (2012). On the effects of frontogenetic strain on symmetric instability and inertia–gravity waves. *Journal of Fluid Mechanics*, *711*, 620–640. https://doi.org/10.1017/jfm.2012.416

Thomas, L. N., Taylor, J. R., Ferrari, R., & Joyce, T. M. (2013). Symmetric instability in the Gulf Stream. *Deep Sea Research, Part II*, *91*, 96–110. https://doi.org/10.1016/j.dsr2.2013.02.025

Vallis, G. K. (Ed.) (2006). *Atmospheric and oceanic fluild Dynamics (Pembroke, Ont.)* (pp. 247–287). Cambridge, UK: Cambridge University Press.